10. Sugars exist as cyclic structures in solution. In H_2O, fructose is about 68% fructopyranose and 32% fructofuranose, and glucose is about 99% glucopyranose and 1% glucofuranose (*24*). In this paper, we use the terms fructose and glucose in reference to the sugars in any of their conformers.
11. M. J. Antal, W. S. L. Mok, G. N. Richards, *Carbohydr. Res.* **199**, 91 (1990).
12. Z. Srokol *et al.*, *Carbohydr. Res.* **339**, 1717 (2004).
13. B. M. Kabyemela, T. Adschiri, R. M. Malaluan, K. Arai, *Ind. Eng. Chem. Res.* **38**, 2888 (1999).
14. B. M. Kabyemela, T. Adschiri, R. M. Malaluan, K. Arai, *Ind. Eng. Chem. Res.* **36**, 1552 (1997).
15. C. Lansalot-Matras, C. Moreau, *Catal. Commun.* **4**, 517 (2003).
16. C. Moreau, A. Finiels, L. Vanoye, *J. Mol. Catal. Chem.* **253**, 165 (2006).
17. Materials and methods can be found on *Science* Online.
18. The [EMIM]Cl in this study gave a pH of 7 when mixed with H_2O in a 1:1 ratio. The pH of less-pure ionic liquids ranged from neutral to acidic.
19. At a mole ratio of 2, the melt is a Lewis acid (*25*).
20. R. C. Remsing, R. P. Swatloski, R. D. Rogers, G. Moyna, *Chem. Commun.* 1271 (2006).
21. $CuCl_2$ was used to study sugar-metal interactions, because chromium is strongly paramagnetic and the line-broadened spectrum was uninformative.
22. Z. C. Zhang, *Adv. Catal.* **49**, 153 (2006).
23. L. Mønsted, O. Mønsted, *Inorg. Chem.* **44**, 1950 (2005).
24. S. J. Angyal, *Adv. Carbohydr. Chem. Biochem.* **42**, 63 (1984).
25. K. M. Dieter, C. J. Dymek Jr., N. E. Heimer, J. W. Rovang, J. S. Wilkes, *J. Am. Chem. Soc.* **110**, 2722 (1988).

26. This work was supported by the Laboratory Directed Research and Development Program at the Pacific Northwest National Laboratory (PNNL), a multiprogram national laboratory operated by Battelle for the U.S. DOE under contract no. DE-AC06-76RL01830. Part of the research described in this paper was performed at the Environmental Molecular Science Laboratory, a national scientific user facility located at PNNL. We thank A. Appel for running the NMR experiments.

Supporting Online Material

www.sciencemag.org/cgi/content/full/316/5831/1597/DC1
Materials and Methods
Figs. S1 to S4

12 February 2007; accepted 18 April 2007
10.1126/science.1141199

Extracellular Proteins Limit the Dispersal of Biogenic Nanoparticles

John W. Moreau,[1]*† Peter K. Weber,[2] Michael C. Martin,[3] Benjamin Gilbert,[4] Ian D. Hutcheon,[2] Jillian F. Banfield[1,4,5]

High–spatial-resolution secondary ion microprobe spectrometry, synchrotron radiation–based Fourier-transform infrared spectroscopy, and polyacrylamide gel analysis demonstrated the intimate association of proteins with spheroidal aggregates of biogenic zinc sulfide nanocrystals, an example of extracellular biomineralization. Experiments involving synthetic zinc sulfide nanoparticles and representative amino acids indicated a driving role for cysteine in rapid nanoparticle aggregation. These findings suggest that microbially derived extracellular proteins can limit the dispersal of nanoparticulate metal-bearing phases, such as the mineral products of bioremediation, that may otherwise be transported away from their source by subsurface fluid flow.

Sulfate-reducing bacteria can lower the concentrations of metals in anoxic waters by sequestering metals into nanoparticles (*1*–*3*). However, these particles are potentially highly mobile because of their small size (*4*) and can redissolve quickly if conditions change (*5*). Sulfide nanoparticles may be <2 nm in diameter [comparable in size to aqueous molecular clusters (*6*)]; most have a diameter of 2 to 6 nm (*2*, *7*). Aggregation can restrict nanoparticle transport by inducing settling (*8*, *9*), and it can drive crystal growth, leading to decreased solubility (*10, 11*). Some organics can promote aggregation. Amine-bearing molecules, for example, have been shown to organize sulfide nanoparticles into semiconductor nanowires (*12*).We investigated the hypothesis that natural organic matter contributes to the formation of densely aggregated nanoparticulate ZnS spheroids and is preserved in nanometer-scale pores (*7*). We used micro-analytical and direct isolation approaches to analyze nanoparticle aggregates formed in natural sulfate-reducing bacterial biofilms (*7*, *13*). We also experimentally evaluated the potential for various amino acids to induce rapid aggregation of metal-sulfide nanoparticles.

We examined sulfate-reducing bacteria–dominated biofilms collected from the Piquette Pb and Zn Mine, a flooded system (pH ~7, ~8°C) in southwestern Wisconsin (*13*). Ultramicrotomed biofilm sections that contained spheroidal aggregates of biogenic ZnS nanoparticles (figs. S1 to S4) were imaged with transmission electron microscopy (TEM) before in situ elemental microanalysis with secondary ion mass spectrometry at a spatial resolution of ~50 nm (NanoSIMS) (*14*). N in the samples was detected by NanoSIMS as CN^-, NO^-, and NS^- secondary ions and was quantified by comparison to reference samples (*14*, *15*).

A comparison of TEM images with NanoSIMS S distribution maps demonstrates that ZnS spheroids are the only structures within the biofilm that contain significant S concentrations (Fig. 1, A to C). The composite NanoSIMS data show the intimate association of N with biofilm ZnS (Fig. 1, A to C); N is present throughout these aggregates at significantly higher levels than in abiotic ZnS reference materials (Fig. 1, D and E). Pores in the ZnS spheroids appear as low–diffraction-contrast features in TEM images because of a lower concentration of sphalerite nanoparticles (fig. S2). Porous regions are associated with the highest N concentrations (Fig. 1, B and C). N concentration measurements for individual spheroids varied by 14% (relative SD, $n = 134$ spheroids), as compared with an average measurement precision of 4%, for individual ZnS aggregates with an average diameter of 700 nm. We estimated an average N concentration for all analyzed biofilm ZnS spheroids of 1.6 weight % (wt %), with a 95% confidence interval of 0.8 to 3 wt % (*14*). By comparison, the average N concentration of synthetic ZnS aggregates was ~100 times lower than it was for biofilm ZnS spheroids.

The small nitrate concentration of mine water (~3 μg/g) was removed from the biofilm during sample processing and was therefore not expected to be the source of N in ZnS. To test this prediction, we analyzed the spheroids for NO^-, relative to CN^- (*14*). The CN^-/NO^- ratio for a reference sample of KNO_3 dissolved in graphite (*14*) ranged from <1 to 200, with a median ratio of ~6. The average CN^-/NO^- ratio of bacterial spores, an organic N reference, was 2950 ± 520 (SD). The average CN^-/NO^- ratio of the biofilm ZnS was 3300 ± 870 (SD). Measurement precision for CN^-/NO^- in the biofilm ZnS was similar to sample variability because of low NO^- secondary-ion intensities. Based on these analyses, we concluded that N in the biofilm ZnS was present neither as nitrate nor nitrite and was therefore organic in nature (*14*). This conclusion was further supported by the presence of amide absorption features in the infrared spectra discussed below. From the average N content of ZnS estimated above and an average amino acid N concentration of ~11 wt %, the ZnS spheroids contained ~14 wt % amino acids.

Areas with cell-like morphologies enriched in N (Fig. 1) and P (fig. S8) are interpreted as being either whole or degraded microbial cells. These features are morphologically distinct from ZnS spheroids, arguing against spheroid formation by nanoparticle encrustation and infilling of cells. We inferred that the spheroids formed by the aggregation of biogenic ZnS nanoparticles (*13*) with extracellular polypeptides or proteins. This process may have involved the adsorption of amino acids or peptides onto nanoparticle surfaces (*16*) or the

[1]Department of Earth and Planetary Science, University of California Berkeley, Berkeley, CA 94720, USA. [2]Glenn T. Seaborg Institute, Lawrence Livermore National Laboratory (LLNL), Livermore, CA 94551, USA. [3]Advanced Light Source, Lawrence Berkeley National Laboratory, Berkeley, CA 94720, USA. [4]Earth Science Division, Lawrence Berkeley National Laboratory, Berkeley, CA 94720, USA. [5]Department of Environmental Science, Policy, and Management, University of California Berkeley, Berkeley, CA 94720, USA.

*Present address: U. S. Geological Survey, Water Resources Division, 8505 Research Way, Middleton, WI 53562, USA. †To whom correspondence should be addressed. E-mail: jwmoreau@usgs.gov

coaggregation of protein molecules and nanoparticles. High N concentrations along the surfaces of some aggregates suggest protein-rich regions (Fig. 1, B and C).

Synchrotron radiation–based Fourier-transform infrared spectroscopy (SR-FTIR), with roughly 10 μm spatial resolution, was used to characterize organics associated with biofilm ZnS aggregates (*14*). SR-FTIR analysis revealed that absorptions at ~1580 and 1640 cm^{-1} were associated only with ZnS spheroid–rich regions of the biofilm (Fig. 2). These absorption features are well described for the amide II and amide I vibration modes, respectively, and they are characteristic of polypeptide- and/or protein-derived amino acids (*17*). Analyses of the spheroid-rich regions of biofilm varied by a few percent in the relative magnitudes of amide I and II absorptions. The SR-FTIR data confirm that the N detected by NanoSIMS analysis of spheroids was organic and support an origin in polypeptides or proteins.

Proteins were directly extracted from density-separated fractions dominated by either organic biofilm components or ZnS spheroids (fig. S6) (*14*). Proteins from the biofilm fraction produced faint bands when reacted with protein-specific stains in 4 to 10% polyacrylamide gels at molecular masses of ~37 and ~48 kD (Fig. 3) (*14*). In contrast, the ZnS-enriched fraction yielded a strong band at ~37 kD, suggesting that the N detected by NanoSIMS and SR-FTIR was associated with protein(s) of this molecular mass. It was not possible to further characterize the protein(s) because of their low concentration and biofilm-sample accessibility (*13*). However, the observed mass lies within the mass range of bacterial proteins known to bind certain metals (*18*–*20*), and genes for these proteins have been reported in some sulfate-reducing bacteria (*21*–*23*). We speculate, therefore, that the ZnS-associated protein(s) found in this study may serve a metal-binding function.

In some aggregates, NanoSIMS data indicated overlapping N and S distributions, implying the presence of fine-scale mixtures of ZnS nanoparticles and protein-rich organic matter. Known bacterial metal-binding proteins bind Zn and other potentially toxic metals (e.g., Cd and Cu), primarily at cysteine residues in proximity to OH^- groups (*24*). Experimental evidence shows that cysteine also binds strongly to ZnS nanoparticles and limits their size to <~5 nm (*25*) and that thiol groups bind strongly with S-deficient surface Fe(II) atoms in pyrite (*16*). The conditional stability constant for monoligand cysteine-Zn^{2+} complexation in low–ionic-strength solutions [≤0.1 moles of charge (M_c)] at 20° to 25°C is more than four orders of magnitude larger than those of all the other amino acids tested except for lysine, for which

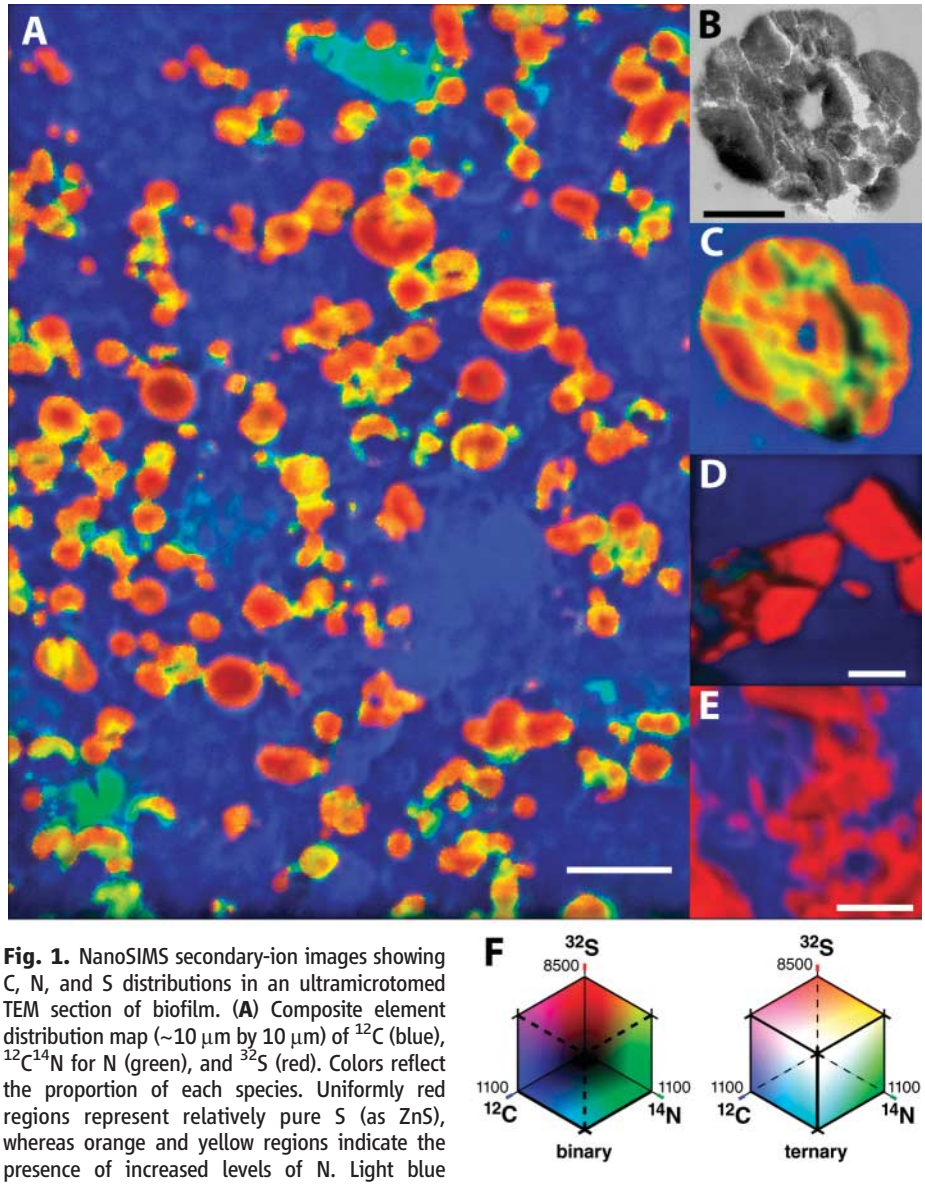

Fig. 1. NanoSIMS secondary-ion images showing C, N, and S distributions in an ultramicrotomed TEM section of biofilm. (**A**) Composite element distribution map (~10 μm by 10 μm) of ^{12}C (blue), $^{12}C^{14}N$ for N (green), and ^{32}S (red). Colors reflect the proportion of each species. Uniformly red regions represent relatively pure S (as ZnS), whereas orange and yellow regions indicate the presence of increased levels of N. Light blue regions indicate the presence of both C and N, with little to no S (no ZnS). (**B**) TEM image of several conjoined ZnS spheroidal aggregates. (**C**) NanoSIMS composite element distribution map of (B). (**D**) NanoSIMS composite element distribution map of ultramicrotomed Balmat ZnS. (**E**) NanoSIMS composite element distribution map of synthetic nanoparticulate ZnS. (**F**) Color box plots of the relative ion abundances displayed in (A) and (C) to (E). Primary colors and maximum ion counts are noted for each species along each axis; all axes are linear, with respect to ion counts. In the left box (binary), only binary ion compositions (one or two species) are shown; in the right box (ternary), only primary (the species corresponding to each axis) and ternary ion compositions (three species) are shown. Black and white corners correspond to points of minimum and maximum ion counts, respectively, for all three species. All scale bars are 1 μm. Figures S8 to S10 (*14*) present grayscale versions of (A), (C), and (D), respectively.

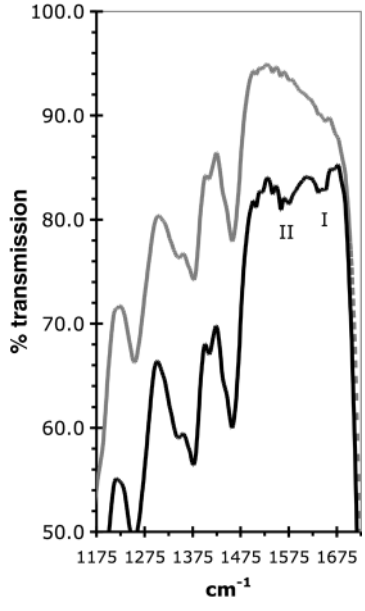

Fig. 2. SR-FTIR transmission spectra of biogenic ZnS aggregates (black) and background biofilm (gray). Amide I (~1640 cm^{-1}) and II (~1580 cm^{-1}) absorption features are diagnostic of amino acid–associated bond vibrations in polypeptides and/or proteins.

the constant is about two orders of magnitude larger (table S1) (*14*). These observations suggest that cysteine or cysteine-rich polypeptides or proteins could have played a role in determining the ZnS particle size and aggregation state.

We tested the efficacy of individual amino acids (100 μM) to promote the aggregation of synthetic ZnS particles 3 nm in diameter or smaller (10 μM) (*14*). The chosen amino acids (alanine, aspartate, cysteine, lysine, phenylalanine, proline, and serine) possess chemically distinct side-chain functional groups. Aggregation was monitored periodically with dynamic light scattering (DLS) (*14*), and results showed that the inorganic aggregation of ZnS initially occurred rapidly to form ~100-nm-diameter aggregates, but then slowed greatly or ceased after 1 week (Fig. 4 and fig. S7). In contrast, ZnS nanoparticles in the presence of cysteine exhibited more extensive and prolonged aggregation, ultimately forming 1-to-10-μm–sized structures. Other amino acids had little (e.g., serine) to no (e.g., proline) detectable effect on nanoparticle aggregation, relative to controls (fig. S7). Cysteine in the absence of ZnS formed no measurable aggregates (Fig. 4), and humic compounds added to ZnS nanoparticle suspensions did not accelerate aggregation.

The DLS results correlate with earlier studies of the adsorption of amino acids, other organic ligands, and inorganic ions onto the surfaces of metal chalcogenides (*16*, *26*, *27*). For example, the sulfhydryl group present in cysteine and mercapto-compounds exhibits strong specific binding to the surfaces of sulfide minerals and nanoparticles. Similarly, serine with a terminal hydroxyl group causes somewhat more aggregation than is observed in control samples, as was expected from both the weaker chemical interaction of this group with sulfide surfaces and the higher pK_a (where K_a is the acid dissociation constant), relative to cysteine (9.15 versus 8.33). Thus, strong specific chemical binding is a necessary prelude to amino acid– or protein-driven ZnS nanoparticle aggregation.

Mineral/protein mixtures with internal organization are typically considered biominerals, and biominerals normally form within organisms. The structures reported here represent an exception to this pattern. Proteins, peptides, and amino acids could be released after cell death and scavenged by hydrophobic ZnS surfaces. Alternatively, bacteria may export Zn-binding proteins for a physiological reason. Most known bacterial metal-binding proteins are produced for intracellular binding and the subsequent export of toxic metals (*24*). In the case reported here, biofilm proteins may bind excess aqueous Zn^{2+} or interact with bound Zn(II) and other proteins after ZnS precipitation. In either scenario, the aggregation of metal-sulfide nanoparticles was promoted, preventing incidental uptake by cells (*28, 29*) or the entombment of cells. From the dense spheroidal morphologies of the aggregates, the rate of aggregation appears to be reaction-limited (*30*). Similar densely packed aggregates of biogenic metal-bearing nanoparticles have been reported from other metal-contaminated systems (*31*). Such aggregates in sediments could trap and possibly preserve organic molecules or their degradation products in sediments or rocks.

Microbial and chemical redox transformations of metals can result in the precipitation of metal-bearing nanoparticles across a range of environmental conditions (*32*). The aggregation state of these particles may have a strong impact on metal mobility and water quality (*33*). Our results suggest that aggregation induced by extracellular metal-binding polypeptides and proteins plays an important role in limiting nanoparticle dispersal in natural environments.

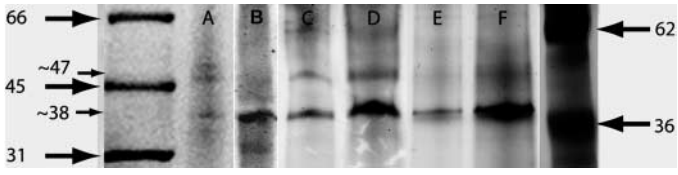

Fig. 3. Composite SDS–polyacrylamide gel electrophoresis image of biofilm and ZnS protein extractions. SyproOrange and colloidal silver molecular weight standards are shown (far left and right lanes, respectively). (**A**) Extraction from the biofilm organic fraction stained with SyproOrange. (**B**) Extraction of the ZnS spheroid fraction stained with SyproOrange. (**C** and **D**) Replicate extractions of the biofilm organic fraction stained with silver. (**E** and **F**) Replicate extractions of ZnS spheroids fraction stained with silver. Numbers are molecular masses in kilodaltons.

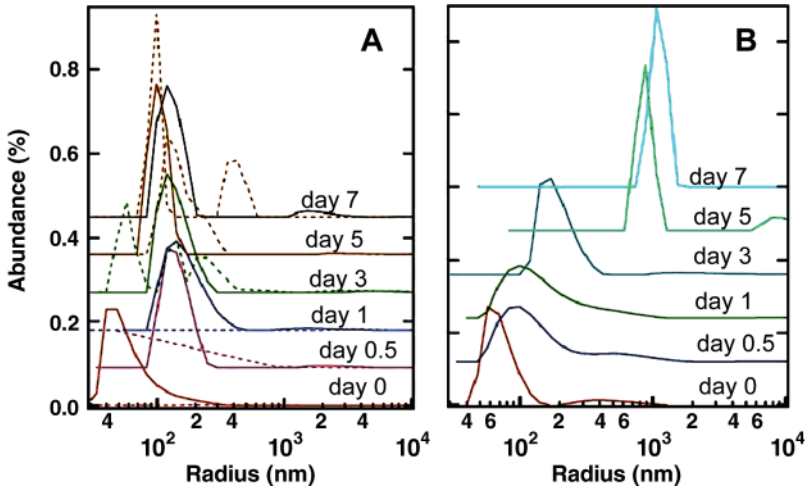

Fig. 4. Size distribution curves from DLS data acquired in ZnS nanoparticle aggregation experiments. (**A**) Control experiments. 10 μM ZnS nanoparticles alone (solid lines) aggregate within 1 day to form ~100-nm-radius clusters that exhibit little further growth over a 5-day period. 100 μM cysteine alone (dashed lines) gives a very weak DLS signal, with no consistent trend in size distribution. (**B**) In the presence of both 10 μM ZnS and 100 μM cysteine, sustained aggregation occurs over the 7-day period, resulting in aggregates that are more than one order of magnitude larger than the initial clusters. DLS correlation functions from which size distributions were derived are shown in fig. S7.

References and Notes

1. J. R. Lloyd, A. N. Mabbett, D. R. Williams, L. E. Macaskie, *Hydrometallurgy* **59**, 327 (2001).
2. Y. Suzuki, S. D. Kelly, K. M. Kemner, J. F. Banfield, *Nature* **419**, 134 (2002).
3. S. L. Hockin, G. M. Gadd, *Appl. Environ. Microbiol.* **69**, 7063 (2003).
4. B. D. Honeyman, *Nature* **397**, 23 (1999).
5. J. G. Hering, W. Stumm, in *Mineral-Water Interface Geochemistry; Reviews in Mineralogy*, vol. 23, M. F. Hochella Jr., A. F. White, Eds. (Mineralogical Society of America, Washington, DC, 1990), pp. 427–465.
6. G. W. Luther, S. M. Theberge, D. T. Rickard, *Geochim. Cosmochim. Acta* **63**, 3159 (1999).
7. J. W. Moreau, R. I. Webb, J. F. Banfield, *Am. Mineral.* **89**, 950 (2004).
8. C. Allain, M. Cloitre, F. Parisse, *J. Colloid Interface Sci.* **178**, 411 (1996).
9. S. A. Bradford, S. R. Yates, M. Bettehar, J. Simunek, *Water Resour. Res.* **38**, 1327 (2002).
10. J. W. Zhang, G. H. Nancollas, in *Mineral-Water Interface Geochemistry; Reviews in Mineralogy*, vol. 23, M. F. Hochella Jr., A.F. White, Eds. (Mineralogical Society of America, Washington, DC, 1990), pp. 365–393.
11. W. Stumm, J. J. Morgan, *Aquatic Chemistry: Chemical Equilibria and Rates in Natural Waters* (Wiley, New York, 1996), pp. 400–414.
12. Q. Lu, F. Gao, D. Zhao, *Nanotechnology* **13**, 741 (2002).
13. M. Labrenz *et al.*, *Science* **290**, 1744 (2000).
14. Materials and methods are available as supporting material on *Science* Online.
15. E. H. Hauri, J. Wang, D. G. Pearson, G. P. Bulanova, *Chem. Geol.* **185**, 149 (2002).
16. J. Bebié, M. A. A. Schoonen, *Geochem. Trans.* **1**, 47 (2000).
17. H. H. Mantsch, D. Chapman, *Infrared Spectroscopy of Biomolecules* (Wiley-Liss, New York, 1996).
18. M. B. Khazaeli, R. S. Mitra, *Appl. Environ. Microbiol.* **41**, 46 (1981).
19. E. Kurek, A. J. Francis, J.-M. Bollag, *Arch. Environ. Contam. Toxicol.* **20**, 106 (1991).
20. D. H. Nies, *J. Bacteriol.* **174**, 8102 (1992).
21. N. Naz, H. K. Young, N. Ahmed, G. M. Gadd, *Appl. Environ. Microbiol.* **71**, 4610 (2005).

22. T. A. M. Bridge, C. White, G. M. Gadd, *Microbiology* **145**, 2987 (1999).
23. C. A. Blindauer *et al.*, *Proc. Natl. Acad. Sci. U.S.A.* **98**, 9593 (2001).
24. B. P. Rosen, *J. Biol. Inorg. Chem.* **1**, 273 (1996).
25. C. L. Torres-Martinez *et al.*, *Nanotechnology* **10**, 340 (1999).
26. L. Ronngren, S. Sjoberg, Z. Sun, W. Forsling, P. W. Schindler, *J. Colloid Interface Sci.* **145**, 396 (1991).
27. W. Vogel, *Langmuir* **16**, 2032 (2000).
28. T. Barkay, J. Schaefer, *Curr. Opin. Microbiol.* **4**, 318 (2001).
29. J. A. Kloepfer, R. E. Mielke, J. L. Nadeau, *Appl. Environ. Microbiol.* **71**, 2548 (2005).
30. G. A. Waychunas, in *Nanoparticles and the Environment; Reviews in Mineralogy and Geochemistry*, vol. 44, J. F. Banfield, A. Navrotsky, Eds. (Mineralogical Society of America, Washington, DC, 1990), pp. 105–166.
31. J. S. Ahn, Y. S. Park, J. Y. Kim, K. W. Kim, *Environ. Geochem. Health* **27**, 147 (2005).
32. M. F. Hochella Jr., *Geochim. Cosmochim. Acta* **66**, 735 (2002).
33. M. S. Diallo, N. Savage, *J. Nanopart. Res.* **7**, 325 (2005).
34. We thank T. Thomsen and colleagues of Diversion SCUBA (Madison, WI) for recovering biofilm samples; Rick and Robyn Webb (University of Queensland, Australia), H. Zhang (University of California, Berkeley), and C. Ramon (LLNL) for assistance in preparing biofilm and synthetic ZnS samples for TEM and NanoSIMS; L. Nittler (Carnegie Institution of Washington, DC) for assistance with processing NanoSIMS data; R. G. Wilson for data on N in ZnS; and M. Thelen and C. Jeans (LLNL) for assistance with protein extractions. The comments of two anonymous reviewers greatly improved the quality and clarity of our manuscript. Work was funded by the U.S. Department of Energy Basic Energy Sciences Program under contract no. DE-FG02-04ER15507, the NASA Astrobiology Institute under contract no. NNA04CC02A (J.W.M. and J.F.B.), and the U.S. Department of Energy Office of Biological and Environmental Research Genomics Genomes to Life research program (P.K.W. and I.D.H.). Work was performed at LLNL under the auspices of the U.S. Department of Energy under contract no. W-7405-Eng-4. The Advanced Light Source is supported by the director of the Office of Science, Office of Basic Energy Sciences, of the U.S. Department of Energy under contract no. DE-AC02-05CH11231.

Supporting Online Material

www.sciencemag.org/cgi/content/full/316/5831/1600/DC1
Materials and Methods
Figs. S1 to S11
Table S1
References

8 February 2007; accepted 4 May 2007
10.1126/science.1141064

Origin of the Low Rigidity of the Earth's Inner Core

Anatoly B. Belonoshko,[1,2]* Natalia V. Skorodumova,[3] Sergio Davis,[1] Alexander N. Osiptsov,[4] Anders Rosengren,[2] Börje Johansson[1,3,5]

Earth's solid-iron inner core has a low rigidity that manifests itself in the anomalously low velocities of shear waves as compared to shear wave velocities measured in iron alloys. Normally, when estimating the elastic properties of a polycrystal, one calculates an average over different orientations of a single crystal. This approach does not take into account the grain boundaries and defects that are likely to be abundant at high temperatures relevant for the inner core conditions. By using molecular dynamics simulations, we show that, if defects are considered, the calculated shear modulus and shear wave velocity decrease dramatically as compared to those estimates obtained from the averaged single-crystal values. Thus, the low shear wave velocity in the inner core is explained.

Since the discovery of Earth's inner core (IC) by Ingrid Lehmann in 1936 (*1*), it has been established, on the basis of the equation of state as compared to seismic data and the abundance of iron, that Earth's IC mainly consists of iron (*2*–*5*). However, the resistance of iron and its alloys to shear, either measured (*6*, *7*) or calculated (*8*), does not match the very low resistance to shear of the IC, as follows from the low velocity of the shear signal propagation (*4*, *9*). To explain the low rigidity of the IC, it has been suggested that Earth's IC contains liquid inclusions (*10*). This suggestion, however, is met with certain difficulties (*11*, *12*), because a liquid is likely to be squeezed out of the IC. Therefore, a satisfactory explanation of the low rigidity of Earth's IC is still lacking. Computational materials physics has now reached a high degree of sophistication and reliability in the calculations of crystal elastic constants at the conditions relevant for the IC (*8*). Yet, the shear moduli of relevant iron alloys, obtained by the most advanced computational methods, are systematically higher than the observed shear modulus of the IC (*8*). This trend makes one question the validity of the procedure currently applied for calculating the elastic constants of materials at high temperature T and pressure P. At present, one calculates the elastic properties of a polycrystalline material by averaging the elastic properties of a single crystal over all possible crystallographic orientations (*13*). Thus, the elastic properties of a polycrystalline material are completely defined by the properties of the single crystal. Although this approach can be quite legitimate at low temperature, it might fail under conditions when grain boundaries become viscous (*14*), which is likely at high temperature.

To investigate the impact of defects and grain boundaries on the shear properties of polycrystalline iron under the IC pressure and temperature conditions and to evaluate the applicability of the contemporary approach to calculate shear properties of iron in Earth's IC, we study the elastic behavior of an ideal iron crystal in comparison with that of a "realistic" sample containing several grain boundaries as well as other extensive structural defects.

Among the possible computational methods, the method of molecular dynamics (MD) appears to be very suitable for calculating the elastic properties of a material at finite temperatures. MD simulations of realistic samples require a large number of atoms that prevents the application of pure ab initio methods. Recently, a sufficiently precise embedded-atom model (EAM) of high-pressure iron has been developed (*15*–*17*).

Table 1. Calculated properties of bcc iron as compared to the IC data.

Parameter (units)	Ab initio (*18*)		EAM (*15*)	Earth's IC (*4*)
P (GPa)	356.7	360.0	360.0	363.9
T (K)	6000.0	6000.0	7400.0	5000 to 8000 (*5*)
B (GPa)	1486.0	1372.7	1380.0	1425.3
C_{11} (GPa)	1561.6	1391.0	1415.1	
C_{12} (GPa)	1448.1	1363.5	1362.5	
C_{44} (GPa)	365.5	448.0	387.0	
G (GPa)	242.0	274.3	243.1	176.1
ρ (g/cm^3)	13.58	13.90	13.78	13.09
V_L (km/sec)	11.54	11.90	11.12	11.26
V_S (km/sec)	4.22	4.44	4.20	3.67

[1]Applied Materials Physics, Department of Materials Science and Engineering, The Royal Institute of Technology, SE-100 44 Stockholm, Sweden. [2]Condensed Matter Theory, AlbaNova University Center, Department of Theoretical Physics, The Royal Institute of Technology, SE-10691 Stockholm, Sweden. [3]Condensed Matter Theory Group, Department of Physics, Uppsala University, Uppsala Box 530, Sweden. [4]Institute of Mechanics, Moscow State University, 142432 Moscow, Russia. [5]School of Physics and Optoelectronic Technology and College of Advanced Science and Technology, Dalian University of Technology, Dalian 116024, China.

*To whom correspondence should be addressed. E-mail: anatoly.belonoshko@fysik.uu.se